NOTICE CONCERNING COPYRIGHT RESTRICTIONS

largest percentage increase in radon entry over time is found. This is the case when the steady-state radon inflow is not too large yet there is appreciable enhancement in advective radon inflow when the pressure is decreasing. The largest predicted increases (for uniform soil permeability) are for the cases $k = 10^{-11}$ m^2 and $T = 0.5$ hr in the dirt basement configuration and $k = 10^{-12}$ m^2 and $T = 24$ hr in the crack configuration. Table 1 shows that the increase in radon inflow is even greater if a high-permeability (10^{-10} m^2) layer is present beneath the concrete slab. This kind of permeability heterogeneity maximizes the effect of the "local" enhancement of the pumping advective radon transport at the basement opening, yet the effective permeability of the total soil mass remains small, since the high-permeability layer constitutes only a small fraction of the total volume; the small effective permeability ensures that steady-state radon inflow due to basement depressurization remains small if the soil permeability is $\leq 10^{-12}$ m^2.

SUMMARY AND CONCLUSION

Study results show that for a homogeneous soil medium, the largest increase in radon entry (over steady-state advective transport with a 5-Pa underpressure at the basement) occurs for $k = 10^{-12}$ m^2 with the barometric variation of period $T = 24$ hr and amplitude 250 Pa in the crack configuration. The increase is 120%. In the dirt floor configuration, the largest percentage increase is 68% over that of steady radon entry with 5 Pa underpressure at the basement for $k = 10^{-11}$ m^2 and a pumping period of 0.5 hr. The increase in radon entry with pumping is further enhanced when there is a heterogeneity in permeability arising from the physical situation of a high-permeability aggregate layer immediately below the basement floor.

The different configurations chosen (dirt floor basement and impermeable basement floor with crack) serve to demonstrate the relative importance of the different transport processes: diffusive, steady-state advective, and pressure-pumping advective. A significant result from this study is that the advective radon transport from pressure pumping may be an order of magnitude larger than the diffusive transport in the absence of a persistent underpressure at the basement, for $k = 10^{-10}$ m^2. This may help to explain indoor radon concentrations during periods of low steady-state driving force.

ACKNOWLEDGMENT

We would like to thank Mohsen Alavi of the Earth Sciences Division of LBL for help in modifying the computer code CHAMP.

REFERENCES

Narasimhan, T.N., Alavi, M., Liu, C.W., 1985. CHAMP—A computer code for modeling transient fluid flow and chemical transport with hydrodynamic dispersion in variably saturated systems. *In* Proceedings of the Symposium on Groundwater Flow and Transport Modeling for Performance Assessment of Deep Geologic Disposal of Radioactive Waste: A Critical Evaluation of the State of the Art. Albuquerque, New Mexico, May 20–21.

Nazaroff, W.W. and Nero, A.V., Jr. (eds.), 1988. Radon and Its Decay Products in Indoor Air. Wiley, New York, p. 57–111.

Nazaroff, W.W., Moed, B.A., and Sextro, R.G., 1988. Soil as a source of indoor radon: Generation, migration, and entry. *In* W.W. Nazaroff and A.V. Nero, Jr. (eds.), Radon and Its Decay Products in Indoor Air. Wiley, New York, p. 57–111.

Tsang, Y.W., and Narasimhan, T.N., 1992. Effects of periodic atmospheric pressure variation on radon entry into buildings. J. Geophys. Res., v. 97, no. B6, p. 9161–9170.

6835

Studies of the Role of Fault Zones on Fluid Flow Using the Site-Scale Numerical Model of Yucca Mountain

C. S. Wittwer, G. Chen, and G. S. Bodvarsson

Lawrence Berkeley Laboratory (LBL) in cooperation with the United States Geological Survey (USGS) has developed a three-dimensional site-scale numerical model of the unsaturated zone at Yucca Mountain, Nevada. The hydrogeology of the site is controlled by fluid flow through heterogenous, unsaturated fractured and porous layers of volcanic tuffs in an arid environment. The site-scale model covers an area of about 30 km^2 around the potential repository area and is bounded by major fault zones to the north (Yucca Wash fault), east (Solitario Canyon fault), and west (Bow Ridge fault). The numerical grid was designed to account for the geological and hydrogeological mechanisms that have been described in the literature as being relevant to moisture flow at Yucca Mountain (Montazer

and Wilson, 1984). Additional data treatment reported in Wittwer et al. (1992) led to the development of a highly nonuniform three-dimensional numerical grid that reproduces both the complex geology of this fractured region and the spatial distribution of hydrogeological units and explicitly includes the offset of the hydrogeological units due to three major fault zones.

This article briefly summarizes results of steady-state simulations published in Wittwer et al. (1993) and performed with two NW to SE cross-sectional submodels extracted from the three-dimensional numerical grid of the site-scale model.

METHODOLOGY

The three-dimensional numerical grid consists of about 5000 elements and 20,000 connections. The horizontal grid for the site-scale model is shown in Figure 1. The vertical grid geometry consists of seventeen nonuniform layers that represent, as closely as possible, lithological variations within the main hydrogeological units; these include extremely massive vitrophyre layers at the border of the main ash flows, the occurrence of lithophysae cavities within the welded units, and the presence of zeolitic alteration. The computer-developed grid also allows one to readily modify and adapt the nonuniform numerical grid to new data or new problems.

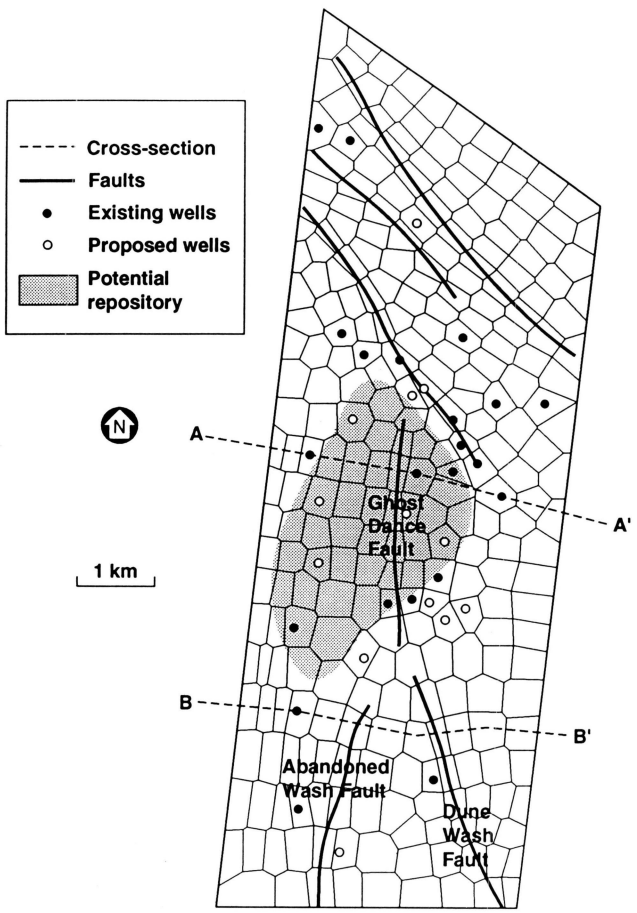

Figure 1. Horizontal grid for the site-scale model showing the two cross-sectional models. [XBL 936-879]

The simulations discussed here were performed with two-dimensional cross sections extracted from the three-dimensional grid. The northern cross section (A-A′) cuts the site-scale model area at the level of the potential repository and includes the Ghost Dance fault (see Figure 1). The second cross section (B-B′) is located about 3 km farther south and intersects the Abandoned Wash and Dune Wash faults.

Representative values shown in Table 1 for the parameters of the rock matrix were compiled from data found in the literature. The values used in the models were chosen on the basis of the distribution of the measured parameter values, the locations of the samples within the different units, and the lithological similarities within each of the hydrogeological layers.

The method developed by van Genuchten (1980) was used to represent the relationship between capillary pressure and liquid saturation, as well as between relative permeability and liquid saturation. New moisture-retention measurements performed on core and surface samples by Flint and Flint (personal communication, 1992) were used in this study, as these represent the best current available data sets.

As a high fracture density has been reported in the literature for the welded units, fracture flow representation was added to the rock matrix characteristic curves for the Tiva Canyon and Topopah Spring hydrogeological units. The equivalent continuum approximation developed by Klavetter and Peters (1986) on the basis of capillary equilibrium between the matrix and the fracture was used to integrate fracture flow to matrix flow.

Because no capillary functions have been reported in the literature for fracture flow, the approach used in the simulations is based on the assumption that the fractured medium has the same pore size distribution as the rock matrix for each rock type. The absolute fracture permeability was taken to be equal to 10^{-11} m^2 on the basis of values reported by Klavetter and Peters (1986). The air entry value is predicted from the saturated permeability value k_s by using the scaling relationship proposed in Wang (1992). The combined fracture and matrix characteristic curves were developed for the layers of the welded Tiva Canyon and Topopah Spring units. These curves show that fracture-dominated flow begins between 1000 and 3500 Pa for the various sublayers. The approach used therefore assumes only matrix flow until very high liquid saturations are reached.

Table 1. Rock matrix properties for the seventeen model layers.

Hydrogeological unit	Lithology	Sub-layer	Porosity Range (%)	Porosity Model (%)	Permeability Range (m^2)	Permeability Model (m^2)	$\alpha \times 10^{-5}$ (Pa)	n	m
Tiva Canyon welded tuff	Caprock Upper cliff	1.1	6 – 24	17	2E-19 – 2E-14	1E-18	0.067	1.33	0.250
	Upper lithophysae Clinkstone Zone								
	Lower lithophysae	1.2	6 – 28	17	1E-20 – 2E-16	2E-18	0.067	1.33	0.250
	Hackly zone Columnar zone								
	Vitrophyre	1.3	2 – 10	6	4E-17 – 1E-15	1E-18	0.067	1.33	0.250
Paintbrush nonwelded tuff	Shardy base	2.1	12 – 54	33	1E-17 – 5E-13	1E-13	1.67	1.20	0.167
	Nonwelded tuffs Bedded tuffs	2.2	18 – 57	37	5E-16 – 5E-12	5E-14	6.00	1.19	0.163
	Nonwelded tuffs	2.3	10 – 55	32	4E-16 – 6E-13	1E-13	4.33	1.17	0.142
Topopah Spring welded tuff	Vitrophyre	3.1	3 – 9	6		1E-18	0.067	1.41	0.290
	Caprock	3.2	9 – 22	15	8E-17 – 4E-14	4E-16	0.125	1.22	0.180
	Rounded zone Upper lithophysae	3.3	10 – 16	13	5E-20 – 3E-18	4E-18	0.20	1.28	0.220
	Middle non-lithophysae	3.4	6 – 22	14	4E-20 – 1E-17	5E-18	0.133	1.33	0.250
	Lower Lithophysae								
	Lower non-lithophysae	3.5	6 – 18	12	4E-20 – 1E-17	5E-18	0.067	1.33	0.250
	Vitrophyre	3.6	1 – 10	5	5E-20 – 2E-17	1E-18	0.067	1.41	0.290
Calico Hills nonwelded tuff	Bedded tuffs	5.1	23 – 48	35	2E-13	2.0	1.15	0.130	
	Nonwelded vitric Bedded tuffs	5.2	8 – 48	28	1E-18 – 2E-15	3E-13	2.0	1.14	0.120
	Nonwelded tuffs Slightly zeolitized	5.3	30 – 48	39		3E-13	2.0	1.14	0.120
	Zeolitized, Partly argillic	5.4	14 – 36	25	5E-19 – 7E-17	1E-16	0.1	1.23	0.190
	Zeolitized, devitrified Zeolitized	5.5							

The three fault zones are represented in the numerical grid by columns of gridblocks about 200 to 350 m in width. In the present study, fault zones were treated as porous media with either very high or very low permeability compared with the neighboring rock matrix. The van Genuchten model was used to calculate the capillary pressure curves, as well as the relative permeability curves, of the fault zones for these two test cases.

RESULTS OF TWO-DIMENSIONAL NUMERICAL SIMULATIONS

Numerical simulations were performed with the computer code TOUGH2 (Pruess, 1990), which is based on the integral finite difference method and which accounts for the transport of moisture, air, and heat in unsaturated porous and fractured media. Capillary pressure and liquid saturation distributions for the two-dimensional vertical cross

sections were calculated for three spatially uniform infiltration rates of 10^{-1} to 10^{-3} mm y^{-1} .

Results for the set of simulations using the maximum infiltration rate of 10^{-1} mm y^{-1} used in this study, are shown in Figure 2a for capillary pressure and in Figure 2b for liquid saturation. The capillary pressure decreases in the Tiva Canyon, down to the middle of the Topopah, where high liquid saturations are reached in a low-permeability layer representing the upper lithophysae zone. The saturation distribution shows distinct features. The liquid saturation in the Tiva Canyon unit decreases with depth. A high-saturation zone occurs at the bottom of the Topopah Spring, just above the water table in the eastern part of the model, and propagates westward at the contact with the Calico Hills vitric layers slightly beyond the Ghost Dance fault. Liquid saturations of the different units vary within well-defined limits: for example, Tiva Canyon (0.97–0.91), Paintbrush (0.78–0.93), Topopah Spring (0.78–0.93), Calico Hills vitric (0.55–0.70), and Calico Hills zeolitic (0.90–0.99). Because of the chosen characteristic curves, low liquid saturations occur in the fault zone when it is modeled as a high-permeability zone. On the contrary, very high saturations occur in high-permeability fault zones.

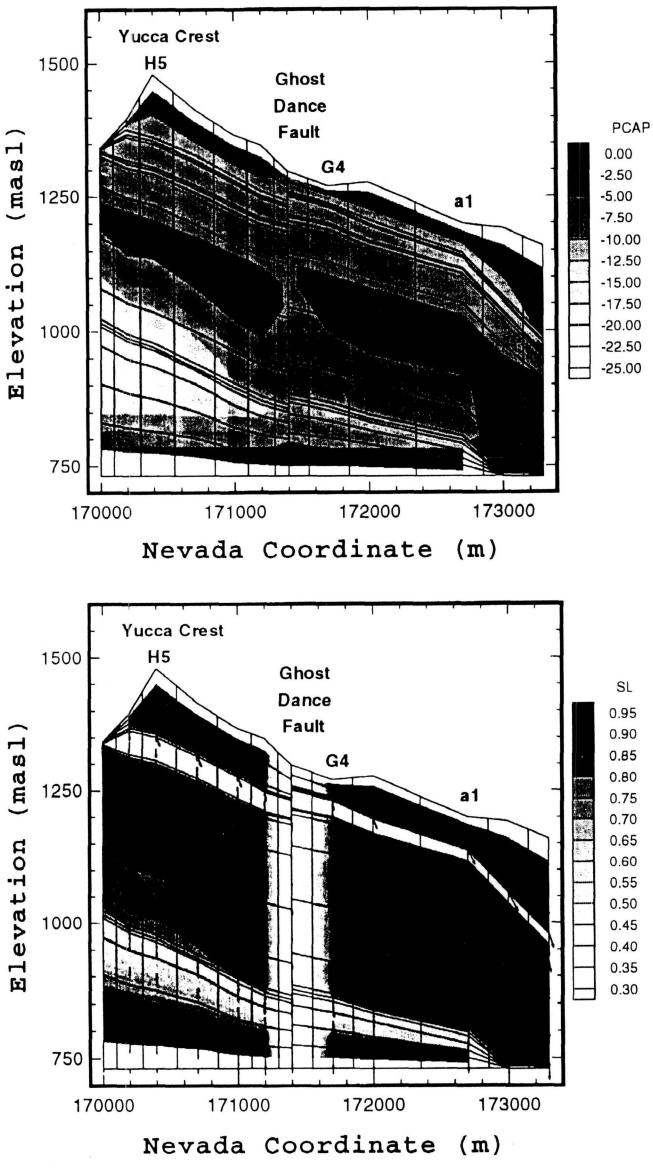

Figure 2. Capillary pressure distribution (**a**) and liquid saturation distributon (**b**) for cross section A-A′ with infiltration rate of 10^{-1} mm y^{-1} and a saturated permeability of 10^{-11} m^2 for the Ghost Dance fault. [XBL 936-880]

The saturation distribution for a decreased infiltration rate of 10^{-2} mm y^{-1} is similar to the previous simulations, but the liquid saturations have decreased to 0.84–0.80 in the Tiva Canyon, 0.40–0.53 in the Paintbrush, and 0.65–0.90 in the Topopah Spring. Numerical simulations were also run to reach steady state with an infiltration rate of 10^{-3} mm yr^{-1}. The capillary pressure distribution obtained for this very low rate does not deviate strongly from static conditions. The liquid saturations in the three upper units have now decreased even further to 0.77–0.67 in the Tiva Canyon, 0.35–0.45 in the Paintbrush, and 0.60–0.85 in the Topopah Spring.

Simulations with cross section B-B′ show the effects of two fault zones (the Abandoned Wash fault and the Dune Wash fault). Except for a few details, the distribution using high- and low-permeability fault zones do not differ significantly from the equivalent cases that include only the Ghost Dance fault.

Lateral flow occurs when the vertical flow is diverted because of the tilting of the layers, and may be enhanced by the permeability contrast. In our simulations, this lateral eastward flow is terminated by the fault zones, because of their assumed flow characteristics. As the intensity of lateral flow depends on the length of the flow path and the volume of the drainage zone, the flows calculated on the eastern side of the Abandoned Wash and Dune Wash faults are smaller than those defined at the Ghost Dance fault.

Vertical flow rates were also studied within the Ghost Dance fault zone. A general feature shows a strong decrease in vertical flow rate with depth in the fault zone, suggesting that water flows into the adjacent formation. This effect seems to be limited to the gridblocks close to the fault zone. The reason for this outflow from the fault zone is, again, the characteristic curves used. High flow within the fault zone results in relatively high capillary pressures, hence the moisture leaves the fault zone for the lower (more negative) capillary pressure of the surrounding rocks.

Outside of the fault zones, vertical flow is dominant, and eastward lateral flow remains about 100 times lower than vertical flow and is even lower in the vitrophyre lay-

ers, which have very low permeability. Increased lateral flow mainly occurs in the top of the Topopah, in the more permeable layer representing the rounded zone. Weaker lateral flow also occurs in the first layer of the Paintbrush unit, just below the very low permeable vitrophyre layer of the Tiva Canyon.

The various simulations show that perched water zones do not occur in the present set of simulations, because of the relatively low infiltration rates used. Potential zones are located in the base of the Topopah Spring, especially east of the Ghost Dance fault.

CONCLUSION

Two-dimensional simulations were carried out to investigate the role of major faults (Ghost Dance, Abandoned Wash, and Dune Wash) on fluid flow within the unsaturated zone of the site-scale model. As hydrological properties of these faults are not known at present, bounding calculations were performed in order to study the effect of the faults. The faults were assumed to have either very high permeability and low potential capillary pressure or very low permeability and high potential capillary pressure. The approach taken in the design of the numerical grid, together with the numerical capabilities of the TOUGH2 simulator, allows one to analyze the results in terms of preferential pathways, lateral flow, and capillary barriers. Future work will include higher infiltration rates and different representations of the fault zones.

Capillary pressure and liquid saturation distributions are obtained for cross sections with one or two fault zones with infiltration rates of 10^{-1} to 10^{-3} mm y^{-1} and high- and low-permeability fault zones. All results are strongly dependent on the characteristic curves chosen for the different rock types. For high infiltration rates, liquid saturations remain in well-defined limits for each of the hydrogeological units (Tiva Canyon, 0.97–0.91; Paintbrush, 0.78–0.93; Topopah Spring, 0.78–0.93; Calico Hills vitric, 0.55–0.70; and Calico Hills zeolitic, 0.90–0.99), and when less water flux is assumed to infiltrate, the range of liquid saturations decreases in the upper three units. Very different saturations are reached in the high- and low-permeabillity fault zones, depending on their characteristic curves. Vertical flow rate is dominant in all simulations, and lateral flow is generally lower than vertical flow. Increased lateral flow occurs in the upper part of the Topopah Spring and the Paintbrush. No perched water zones were created during the current set of simulations.

In the case of a permeable fault, the assumed characteristic curves result in relatively high (less negative) capillary pressures and very low liquid saturations at steady state. This in turn prevents the entry of flow from neighboring formations into the fault, and in fact some of the infiltration prescribed on the top of the fault is lost to those surrounding rocks. One would get significant vertical flow in a fault only if its properties are such that the characteristic curves are similar to those of the adjacent formations (i.e., not much lower air entry value) and the absolute saturated permeability is significantly larger.

ACKNOWLEDGMENT

The authors appreciate the contributions of M. Chornack, A. Flint, L. Flint, E. Kwiclis, and R. Spengler, U.S. Geological Survey, to this work.

REFERENCES

Klavetter, E.A., and Peters, R.R., 1986. Estimation of hydrologic properties of an unsaturated fractured rock mass. Sandia National Laboratories Report SAND84-2642.

Montazer, P., and Wilson, W.E., 1984. Conceptual hydrologic model of flow in the unsaturated zone at Yucca Mountain, Nevada. Water Resources Investigations Report 84-4355, U.S. Geological Survey.

Pruess, K., 1990. TOUGH2-A general-purpose numerical simulator for multiphase fluid and heat flow. Lawrence Berkeley Laboratory Report LBL-29400.

Pruess, K., Wang, J.S.Y., and Tsang, Y.W., 1990. On thermohydrological conditions near high-level nuclear wastes emplaced in partially saturated fractured tuff, Part 2. Effective continuum approximation. Water Resour. Res., v. 26, no. 6, p. 1249–1261.

van Genuchten, M.Th., 1980. A closed-form equation for predicting the hydraulic conductivity of unsaturated soils. Soil. Sci. Soc. Am. J., v. 44, p. 892–898 .

Wang, J.S.Y., 1992. Variations of hydrological parameters of tuff and soil. Proceedings, Third International Conference on High-Level Radioactive Waste Management, Las Vegas, Nevada, April 12–16, p. 727–731.

Wittwer, C.S., Bodvarsson, G.S., Chornack, M.P., Flint, A.L., Flint, L.E., Lewis, B.D., Spengler, R.W., and Rautman, C.A., 1992. Design of a three-dimensional site-scale model for the unsaturated zone at Yucca Mountain, Nevada. Proceedings, Third International High Level Radioactive Waste Management Conference, Las Vegas, Nevada, April 12–16, p. 263–271.

Wittwer, C.S., Chen, G., and Bodvarsson, G.S., 1993. Studies of the role of faults on fluid flow using the site-scale numerical model of Yucca Mountain. Submitted for publication in the Proceedings of the Fourth International High Level Radioactive Waste Management Conference, Las Vegas.